

# Transient pressure drops of gas bubbles passing through liquid-filled microchannel contractions: an experimental study

Henry Chio<sup>1</sup>, Mads Jakob Jensen<sup>2</sup>, Xiaolin Wang<sup>1</sup>,  
Henrik Bruus<sup>2</sup> and Daniel Attinger<sup>1,3</sup>

<sup>1</sup> Department of Mechanical Engineering, SUNY at Stony Brook, NY 11794-2300, USA

<sup>2</sup> MIC—Department of Micro and Nanotechnology, DTU Bldg 345 East, Technical University of Denmark, DK-2800 Kgs Lyngby, Denmark

E-mail: [da2203@columbia.edu](mailto:da2203@columbia.edu)

Received 29 June 2005, in final form 11 October 2005

Published 13 December 2005

Online at [stacks.iop.org/JMM/16/143](http://stacks.iop.org/JMM/16/143)

## Abstract

We present the first transient pressure measurements and high-speed visualization of gas bubbles passing through liquid-filled microchannel contractions. We have studied contractions ranging from 100 to 500  $\mu\text{m}$  in glass tubes of main diameter 2 mm and compared the experimental results with the recent model of quasi-stationary bubble motion by Jensen, Goranović and Bruus (2004 *J. Micromech. Microeng.* **14** 876) valid for low flow rates. The influence of the wetting angle is studied by coating a tube with a hydrophobic solution. Transient pressure measurements, bubble deformations and the influence of the bubble length on the so-called clogging pressure  $\Delta P_c$  are shown to be in good agreement with the model, both in terms of maximum values and in terms of transient evolution. Some deviations from the model are also observed and possible reasons for these are investigated, such as (a) contact line pinning, (b) thin liquid film along the bubble modifying capillary pressure and (c) viscous pressure drop in the contraction. Experiments with increasing flow rates show that two regimes govern the pressure transients of the bubbles passing the contractions: a quasi-stationary regime for low capillary number and a viscosity-influenced regime for non-negligible capillary numbers. We propose a criterion based on a modified capillary number to discriminate between these two regimes.

## 1. Introduction

In a typical microfluidic system [1], the fluid flows into channels with diameters ranging from 3 mm to 50  $\mu\text{m}$ , along a path involving multiple branching and contractions. The cross section of these channels is either round (tubing) or rectangular (due to microfabrication techniques), with some branching, e.g., in the valving part. Materials range from ceramic and stainless steel to polymer (PTFE, Tygon, Peek) and silicon, each having different wetting properties. There are a number of examples where the functionality of a microfluidic system relies on the presence of gas bubbles such as micropumps

using bubbles as actuators [2], devices where drops are used as chemical reactors [3], devices creating controlled liquid–liquid emulsions [4], and especially liquid–gas emulsions [5–8]. However, in other cases unwanted bubbles may appear in microfluidic systems due to cavitation, electrochemistry or priming (filling) of the microchannels, and they may become problematic if they get stuck in contractions, which are present in the microfluidic system due to some functionality such as valves, tree branching or nozzles. For instance, when a bubble is stuck in a corner or in a dead-flow zone, it can be extremely difficult to dislodge it, resulting in a reduction in dynamic performance or accuracy of the microfluidic device. Therefore, an entire batch of MEMS microfluidic devices can be ruined by only one problematic geometric feature. These problems were already identified a

<sup>3</sup> Present address: Department of Mechanical Engineering, Columbia University, New York NY 10027, USA.

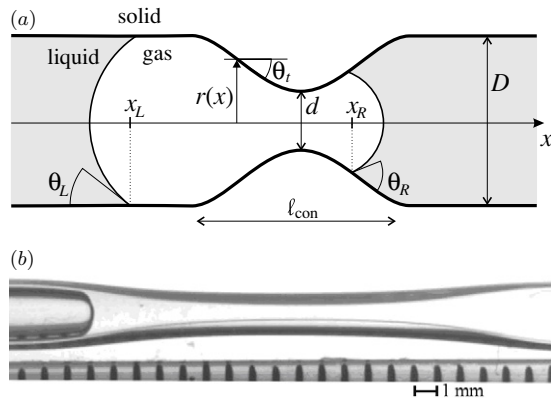


**Figure 1.** (a) Sketch of the gas–liquid–solid system with channel profile  $r(x)$ , main diameter  $D$ , contraction diameter  $d$ , left and right contact angles  $\theta_L$  and  $\theta_R$ , left and right contact line positions  $x_L$  and  $x_R$ , length of the contraction  $\ell_{\text{con}}$  and local tapering angle  $\theta_t$ . (b) Photograph of a gas bubble (dark gray) entering from the left into a liquid-filled (white) tube with a  $490 \mu\text{m}$  contraction. The flow rate  $Q$  of the liquid is  $0.33 \mu\text{l s}^{-1}$ .

decade ago [9, 10], but were not studied in depth before the problem was picked in the recent theoretical study of Jensen, Goranović and Bruus [11].

The pressures needed to move a bubble through a contraction of minimum diameter  $d$ , filled with a liquid of viscosity  $\mu$  and surface tension  $\sigma$ , are related to the laminar friction and the free surface forces. In the laminar regime, the friction contribution for flow rates  $Q$  is proportional to  $\mu Q \ell_{\text{con}} / d^4$ , where  $\ell_{\text{con}}$  is the contraction length, while the free surface contribution due to the Young–Laplace pressure is non-zero and proportional to  $\sigma / d$  as soon as the tube diameter or its wetting properties changes [12]. The resulting pressure transient may be several kPa, and if the bubbles are large enough to span across the microchannel this may block the flow. The minimal external pressure needed to drive such bubbles out of the channel is called the clogging pressure  $\Delta P_c$ . The goal of our work is to contribute to the solution of this important technological problem by studying bubble dynamics in a well-defined microchannel contraction. We begin by presenting the experimental setup and describe the measurement method. Then we give a short review of the theoretical and numerical models used. We move on to compare and discuss the numerical and experimental results, and finally we give some concluding remarks.

**Table 1.** List of the tubes used in this work: tube ID, the main diameter  $D$ , the contraction diameter  $d$ , bubble length  $L$ , measured and simulated clogging pressures  $\Delta P_c^{\text{m}}$  and  $\Delta P_c^{\text{s}}$ , respectively, and the relative deviation DEV between them defined as  $\text{DEV} = (\Delta P_c^{\text{s}} - \Delta P_c^{\text{m}}) / \Delta P_c^{\text{m}}$ .

ID	$D$ (mm)	$d$ ( $\mu\text{m}$ )	$L$ (mm)	$\Delta P_c^{\text{m}}$ (Pa)	$\Delta P_c^{\text{s}}$ (Pa)	DEV (%)
A7	1.78	490	0.6	330	420	21
			3.1	420	500	16
			13.8	420	500	16
A8	1.70	264	1.1	877	790	−11
			4.7	877	750	−17
			12.0	877	840	−4
A19	1.83	103	1.5	2720	2400	−13
			3.1	2720	2410	−13
			3.5	2720	2670	−2
			10.0	2720	2450	−11
A27	2.20	196	4.0	460	510	10

## 2. Capillaries and experimental setup

For the experimental part of the work, different capillary glass tubes of circular cross section were used, see table 1. The tubes with contractions as shown in figure 1 were manufactured in the glass shop of Stony Brook University. We only work with smooth contractions, thereby avoiding problems with cavitation as seen in microfluidic systems with sudden contractions [13]. The tubes have typical internal main diameters  $D = 2 \text{ mm}$  and contraction diameters  $d$  ranging between 100 and  $500 \mu\text{m}$ . In a given experiment, a single capillary tube was connected via stiff polymer (FEP) connection tubes to a syringe pump and a large reservoir, as shown in figure 2.

A single bubble was inserted in the tube and moved at steady flow rates ranging from  $0.1$  to  $200 \mu\text{l s}^{-1}$ . Most experiments were performed at  $0.33 \mu\text{l s}^{-1}$  to keep the laminar friction contribution to the pressure drops negligible. A MEMS-based piezoresistive differential pressure sensor (Honeywell 143PC03D) was connected through a Y-connection between the syringe pump and the tube. After calibration with a digital pressure controller (Druck DPI 530) accurate to  $0.1\%$  full scale, it measured the pressure difference across the bubble in a range of  $\pm 17 \text{ kPa}$ , with a response time of  $1 \text{ ms}$  and a resolution of  $\pm 20 \text{ Pa}$ . The pressure signal was acquired with an HP multimeter and Labview, at a maximum

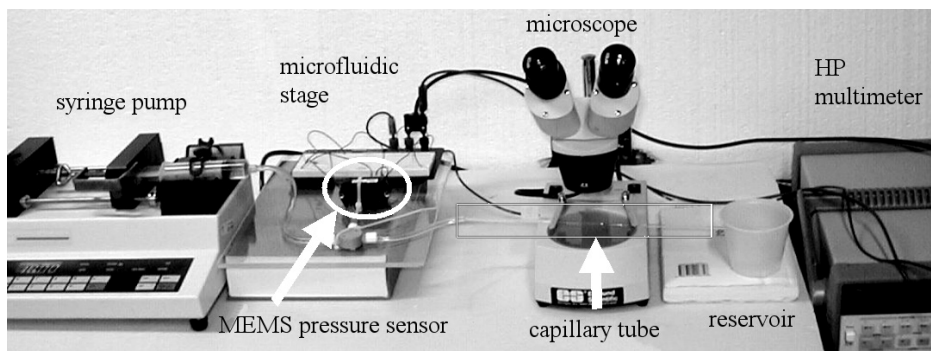


**Figure 2.** Measurement setup allowing for transient visualization and pressure measurement during the transport of a microbubble in a microchannel.

sample rate of 100 Hz. The motion of the bubble was observed either through the stereo microscope visible in figure 2 or through a microscope objective and a Firewire high-speed camera.

While performing experiments several precautions were taken to ensure that the measurements were reproducible. The interior of the glass tubes was soaked in a solution of 5% Contrad (Fisher Scientifics) overnight and then abundantly rinsed with deionized water. No other solvents nor alcohol were put in the tubes as any residue might change surface properties, e.g., the wetting angle. The water used in the experiments was deionized with a Millipore Milli-DI purification system. The wetting angle was measured for a bubble at equilibrium and for velocities corresponding to flow rates of 17.0, 3.33 and 0.33  $\mu\text{l s}^{-1}$ . The geometry of the tubes was measured from the camera pictures and corrected for the magnification effect induced by the curved walls of the glass tube. The latter effect was tested by matching the volume injected in the tube with the experimental and numerical positions of the left and right menisci of the bubble.

### 3. Theory and modeling

A theoretical frame for interpreting our experimental results is provided by implementing the model for quasi-stationary motion of a gas bubble in a microchannel contraction discussed by Jensen, Goranović and Bruus [11] and adapting it to the channel geometries discussed in this paper. We find that this simple model is in good agreement with most of our observations, and in the cases of deviations from experiments it is used as a starting point for pointing out possible theoretical improvements.

On the basis of a microscope picture of a given tube, a spline was fitted to obtain the shape  $r(x)$  of the contraction, see figure 1. This shape is in turn used for numerical prediction of the pressure  $\Delta P_b(x) = P_{\text{in}} - P_{\text{out}}$  across a bubble as a function of its position, where  $P_{\text{in}}$  and  $P_{\text{out}}$  are the pressures at the tube inlet and outlet, respectively, the latter being atmospheric pressure. A bubble is defined by its volume  $V_b$  and the value of the receding (left) and advancing (right) contact angles,  $\theta_L$  and  $\theta_R$ , at the contact lines of the left and right menisci, respectively. The total pressure drop  $\Delta P_b$  can be written in terms of the pressure drops  $\Delta P_\sigma$ , due to capillary forces (simulated by the above-mentioned model), and  $\Delta P_{\text{fric}}$ , due to laminar flow friction,

$$\begin{aligned} \Delta P_b &= P_{\text{in}} - P_{\text{out}} = \Delta P_\sigma + \Delta P_{\text{fric}} \\ &= 2\sigma \left[ \frac{\cos[\theta_R - \theta_t(x_R)]}{r(x_R)} - \frac{\cos[\theta_L - \theta_t(x_L)]}{r(x_L)} \right] \\ &\quad + \alpha\beta \frac{128\mu\ell_{\text{con}}}{\pi d^4} Q, \end{aligned} \quad (1)$$

where  $\theta_t(x)$  is the local tapering angle of the tube shape  $r(x)$ ,  $\alpha$  is a factor close to unity that depends on the shape of the contraction,  $\beta$  is a constant between unity (for a bubble outside the contraction) and zero (for a bubble spanning the contraction) and  $\ell_{\text{con}}$  is the length of the contraction.

For most of the measurements in this paper, the flow rate is so low,  $Q = 0.33 \mu\text{l s}^{-1}$ , that the contribution  $\Delta P_{\text{fric}}$  is negligible. This is verified by noting that when the gas bubble

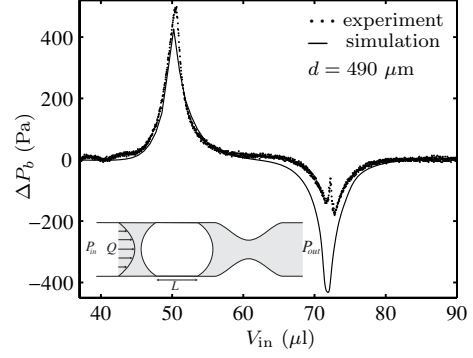


**Figure 3.** Direct measurements with the MEMS pressure sensor (dots) and simulation based on measured shape (full line) of the pressure across a long  $L = 8$  mm bubble in tube A7 for  $Q = 0.33 \mu\text{l s}^{-1}$  as a function of displaced liquid volume  $V_{\text{in}} = Qt$ , where  $t$  is the time. The differential pressure sensor measures  $\Delta P_b = P_{\text{in}} - P_{\text{out}}$ . The observed values of the advancing and receding wetting angles used for the simulations are  $10^\circ$  and  $9^\circ$ , respectively. The inset indicates the bubble length  $L$ , the liquid flow rate  $Q$  and the pressures  $P_{\text{in}}$  and  $P_{\text{out}}$ . The positive and negative pressure peaks occur during the passage through the contraction of the right and left menisci, respectively.

is not in the contraction the Young–Laplace pressure drop at the two menisci cancels, and  $\Delta P_b = \Delta P_{\text{fric}}$ . Direct measurements in this case yield  $P_{\text{fric}} = 3, 24$  and  $482$  Pa for tubes A7, A8 and A19, respectively. Clearly,  $P_{\text{fric}}$  can be neglected for the wide tubes A7 and A8, but not for the narrow tube A19. This issue is discussed further in section 4.5.

### 4. Results and discussion

In the following, we present and discuss our results in five parts: transient pressure and interface curvature, transient pressure and bubble breakup, clogging pressure as a function of tube diameter, influence of wetting angle and influence of flow rate.

#### 4.1. Transient pressure and interface curvature

In figure 3 are shown the measured and simulated pressure drops  $\Delta P_b(x) = P_{\text{in}} - P_{\text{out}}$  across the bubble, according to the definition of equation (1), as a function of the displaced liquid volume in the tube. Two peaks are seen: a positive one at  $V_{\text{in}} \approx 51 \mu\text{l}$  and a negative one at  $V_{\text{in}} \approx 72 \mu\text{l}$ . They correspond to the passage through the contraction of the left and right bubble menisci, respectively. Before and after the two menisci have passed the contraction, the pressure difference across the bubble nearly vanishes, because the advancing and receding wetting angles are equal at such low capillary number, and only the very small laminar viscous contribution remains.

In the simulation, the two peaks are symmetrical. For the first peak, the agreement between the measured and simulated pressures is good. Peak heights (within 20%), widths ( $5 \mu\text{l}$ ) and shapes are comparable.

As we shall discuss here, and again in section 4.4, the magnitude of the second (negative) pressure peak is much smaller in the measurement than in the simulation, and a small pressure spike is visible around  $72 \mu\text{l}$ . Two possible reasons

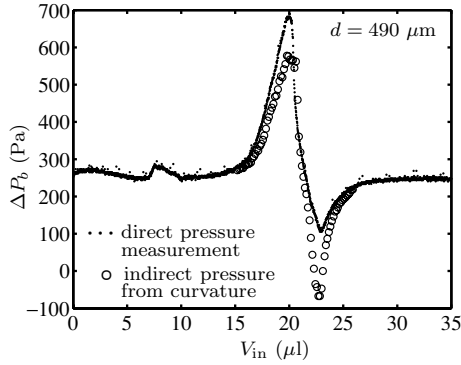


**Figure 4.** Direct measurements with the MEMS pressure sensor (black circles) and calculation from measured curvatures (white circles) of the pressure across a short  $L = 1$  mm bubble. The tube and flow conditions are the same as in figure 3.

for these are (1) that the rear meniscus of the bubble is pinned by interactions with impurities on the glass surface or by interactions with a film left by the front meniscus and (2) that a thin liquid film between the bubble and the glass participates significantly in the pressure drop. Since the measured values of the advancing and receding wetting angles were relatively low (respectively,  $10^\circ$  and  $9^\circ$ , without influence of the velocity), it appears that our system can be considered as hydrophilic. It is therefore worth investigating if a thin water film is formed along the bubble and interacts with the two menisci of the moving bubble. The thickness  $h$  of a film left behind a fully wetting meniscus moving at velocity  $U$  with low capillary number  $Ca = \mu U / \sigma$  in a tube of radius  $r$  can be described by the Bretherton law [14]

$$\frac{h}{r} \propto Ca^{\frac{2}{3}}. \quad (2)$$

For tubes with diameters of 2.0 to 0.1 mm and flow rate  $0.33 \mu\text{l s}^{-1}$ , the meniscus velocity is  $U = 0.1$  to  $40 \text{ mm s}^{-1}$  and  $Ca = 10^{-6}$  to  $5 \times 10^{-4}$ . The thickness  $h$  of the water film left behind is therefore between 200 and 600 nm. The existence of such a liquid film was shown by measuring the passage of electrical current in the saline solution film along a bubble-occluded contraction by Geng *et al* [15].

The first hypothesis, i.e., that the rear meniscus is flattened by pinning, has been tested by measuring with a high-speed camera the temporal evolution of the menisci curvatures. In figure 4, the pressure calculated from the meniscus curvature (white circles) is compared with the direct pressure measurement (black circles). The symmetrical shape of the indirect pressure curve is a good sign that flattening of the meniscus is not responsible for the dissymmetry in the peaks of the direct pressure curve measured with the MEMS pressure sensor. However, when the tube is contaminated, we have observed flattening of the rear meniscus and a corresponding change in measured pressure. This stick–slip motion of the meniscus corresponds to a sawtooth profile of the measured pressure across the bubble.

The second hypothesis, i.e., interactions with a thin film, has been tested to some extent by observing interferences of white light with the bubble–tube contact surface. A diffraction pattern was observed and evolved to a steady pattern over a time of approximately 60 s: this transient phenomenon is likely

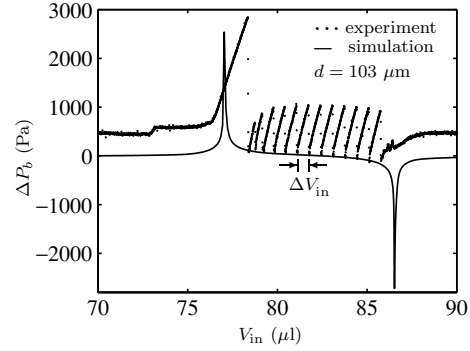


**Figure 5.** Measurements (dots) and simulation (full line) of the pressure drop  $\Delta P_b$  across an  $L = 3.1$  mm bubble in tube A19 for  $Q = 0.33 \mu\text{l s}^{-1}$  as a function of displaced liquid volume  $V_{in} = Qt$ . Note that this tube has the most narrow contraction ( $d = 103 \mu\text{m}$ ) studied in this work. The viscous pressure drop, neglected in the modeling, is now significant and explains the difference in the base level of the two curves. Between the positive and negative pressure peaks, the measured sawtooth-shaped pressure curve has a nearly constant period denoted by  $\Delta V_{in} = 0.54 \mu\text{l}$ .

to indicate the presence of a thin film and its dewetting. It has been shown by Redon *et al* [16] that such a thin film contracts or dewets as a function of viscosity  $\mu$ , surface tension  $\sigma$  and contact angle  $\theta$  with the approximate contraction velocity  $V$  given by

$$V = \frac{1}{120\sqrt{2}} \frac{\sigma}{\mu} \theta^3, \quad (3)$$

provided that the film thickness  $h$  is much smaller than a critical film thickness  $h_c = 2\lambda_{\text{cap}} \sin(q/2) = 400 \mu\text{m}$ , where  $\lambda_{\text{cap}} = 2.7 \text{ mm}$  is the capillary length. In our case, the film thickness is indeed much smaller than  $h_c$ . For the water–glass system, we obtain  $V = 2 \text{ mm s}^{-1}$ . During the observed dewetting time of approximately 60 s, the meniscus in our experiments travels a distance between 6 mm (in the main channel) and 2400 mm (in the smallest contraction). Interactions between the dewetting film, its geometry or disjoining pressure [17] and one of the two bubble menisci are therefore very likely and might be responsible for discrepancies between the measured and simulated pressures, as in figure 3, but these considerations are outside the scope of this study. It must be noted that a laser fringe probing has recently been used to quantitatively monitor the liquid film thickness along a bubble in a liquid-filled capillary [18].

#### 4.2. Transient pressure and bubble breakup

Experiments have been made with a tube exhibiting a more narrow contraction (tube A19,  $110 \mu\text{m}$  contraction), as shown in figure 5. The viscous pressure drop, neglected in the modeling, is now significant and explains the difference in the base level of experimental and theoretical curves. The magnitude of the first pressure peak is comparable with the numerical simulation; however, the shape is not in a good agreement with the simulation. Also, oscillations of the pressure occur at well-defined volume steps  $\Delta V_{in}$  during the entire phase where the bubble is spanning the contraction. The discrepancy in the shape of the first pressure peak can be explained by the fact that our measurement system is not

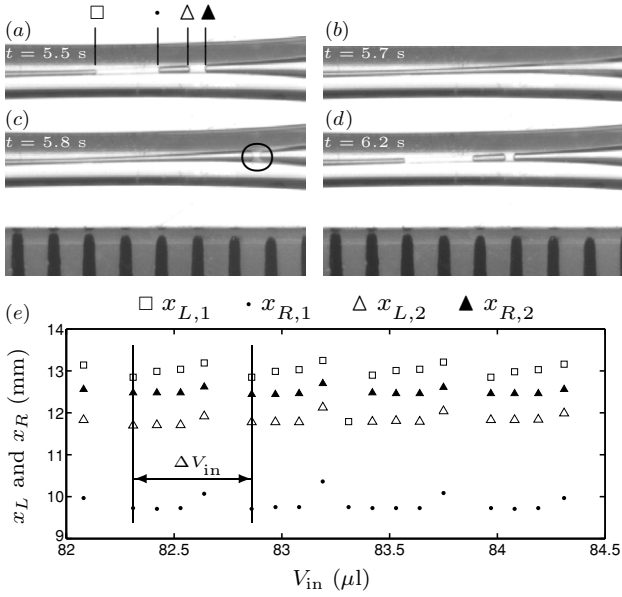


**Figure 6.** (a)–(d) Pictures of an  $L = 1$  mm bubble advancing in tube A19 under the same flow conditions as in figure 5. The positions  $x_{L,1}$ ,  $x_{R,1}$ ,  $x_{L,2}$  and  $x_{R,2}$  of the left and right menisci are indicated on the snapshots extracted from a visualization at 600 fps. The circle in snapshot (c) at time  $t = 5.8$  s shows the initiation of the instability generating the menisci. (e) The positions are plotted as a function of  $V_{in}$ . The vertical lines to the right of the gaps in the measurement points represent the start and end of a period. The size  $\Delta V_{in} = 0.54 \mu\text{l}$  of the periods was observed to be uniform and to coincide with the oscillations in figure 5. The gaps, such as that at  $82.75 \mu\text{l}$ , indicate the reconnection into a single bubble and the corresponding disappearance of the intermediate menisci.

infinitely stiff. We have measured that the volume of our measurement system increases by about  $1 \mu\text{l}$  per kPa internal pressure. Although this deformation is negligible with respect to the overall system volume of about  $12\,000 \mu\text{l}$ , it is enough to reduce the ascending slope of the first pressure peak observed in figure 5 and correspondingly delay the occurrence of the positive pressure peak.

The sawtooth pressure profile is due to instabilities occurring when the bubble passes through a long contraction with large aspect ratio: the single bubble breaks into several smaller bubbles that can merge back and separate with a given frequency. This mechanism is shown in figure 6, where the positions of these sub-bubbles have been visualized with our high-speed camera at 600 fps and measured. This instability involves the creation and destruction of interfaces and induces sawtooth perturbations in the pressure measurement. Comparison between figures 5 and 6 shows a good agreement in terms of the period  $\Delta V_{in} = 0.54 \mu\text{l}$  of the perturbation. It is not known for now if the breakup is due to the elongated shape of the contraction itself or due to the large diameter ratio.

#### 4.3. Clogging pressure as a function of tube diameter

The clogging pressure  $\Delta P_c$  is defined as the minimum pressure needed to push a bubble through the contraction [11]. We have measured the clogging pressures for four different micro-tubes with contractions and for different lengths  $L$  of the bubbles. The results are summarized in table 1.

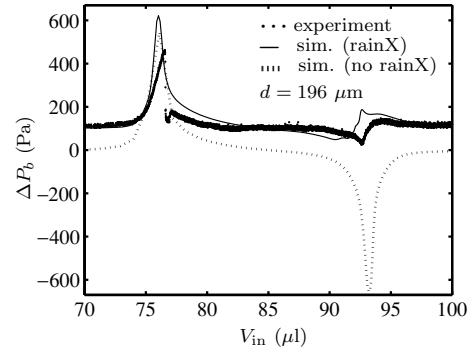


**Figure 7.** Measured (dots) and simulated (full and dotted line) pressure drops  $\Delta P_b$  across an  $L = 4$  mm bubble for  $Q = 0.33 \mu\text{l s}^{-1}$  as a function of displaced liquid volume  $V_{in} = Qt$ . The bubble moves in tube A27 covered with a hydrophobic layer of rainX, and the observed wetting angles used in the simulation are  $\theta_R = 39^\circ$  and  $\theta_L = 89^\circ$ . For comparison is shown a simulation (dashed line) based on the wetting angles for the untreated (hydrophilic) tube.

The tubes have contraction diameters  $d$  between 103 and  $490 \mu\text{m}$ , and the corresponding range of clogging pressure  $\Delta P_c$  is from 2.7 to 0.3 kPa. The experimental and numerical pressure values agree within 20%. For a given contraction, the amplitude of the first pressure peak is constant for bubbles larger than the contraction length. For small bubbles, this is no longer true since both menisci are in the contraction when the pressure reaches its maximum value [11].

#### 4.4. Influence of wetting angle

The influence of the wetting angle was tested by coating the inside of a tube, A27, with a hydrophobic layer of rainX and passing an  $L = 4$  mm bubble through this tube. As seen in figure 7, the measured and simulated pressure drops are in agreement. The simulated curve is based on the measured wetting angles:  $\theta_R = 39^\circ$  and  $\theta_L = 89^\circ$ . In both simulation and experiments, the first pressure peak is much larger than the second, and the qualitative features of the first and second peaks are well matched. The numerical simulation with wetting angles corresponding to a non-coated tube is also plotted for comparison, and it shows large discrepancies with the other two curves.

The better agreement between theory and experiment observed in figure 7 as compared to figure 3 may be understood in terms of the theoretical results obtained by de Gennes *et al* [19] regarding the formation of a thin wetting film. This theory shows that for an increased contact angle, as the  $39^\circ$  in figure 7, a wetting film only arises at higher velocities, while a wetting film is formed more easily at the lower contact angle, such as the  $10^\circ$  in figure 3. Thus, our theoretical model leaving out the wetting film may be more adequately applied for systems with large contact angles.

#### 4.5. Influence of the liquid flow rate

A long  $L = 10$  mm bubble was moved in tubes A7, A8 and A19 with contraction diameters of 490, 103 and  $264 \mu\text{m}$ , respectively, at flow rates ranging from 0.1 to  $160 \mu\text{l s}^{-1}$ . The maximum amplitudes  $|\Delta P|$  of the positive and negative

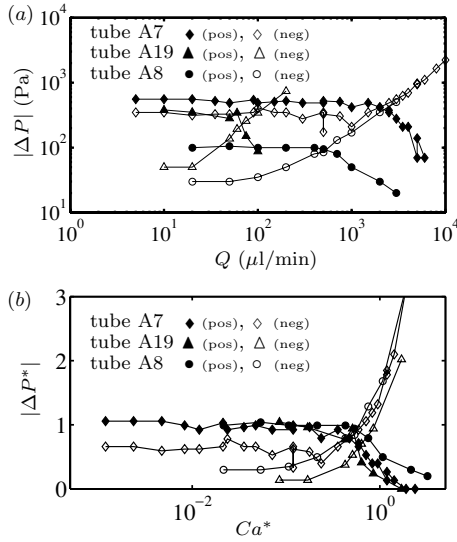


**Figure 8.** (a) Maximum amplitudes  $|\Delta P|$  of the positive (pos) and negative (neg) pressure peaks observed as the bubble passes through the contraction versus flow rate  $Q$  for a long  $L = 10$  mm bubble in tubes A7, A8 and A19 with contraction diameters of 490, 103 and 264  $\mu\text{m}$ , respectively. (b) Same data as in panel (a), but now expressed in terms of the rescaled variables  $\Delta P^*$  versus  $Ca^*$ ; see equations (8) and (7). The negative pressure peak is represented by the open symbols and the positive pressure peak by the filled symbols.

pressure peaks observed as the bubble passes through each contraction are plotted in figure 8(a) as a function of the flow rate  $Q$ .

Two regimes are visible in the figure. (i) For flow rates smaller than a critical value, which depends on the contraction diameter, the positive and negative pressure peak amplitudes are constant, the positive peak being slightly larger than the negative one, as, e.g., in figure 3. (ii) For flow rates larger than the critical value, the amplitude of the positive pressure peak decreases and ultimately vanishes, while the value of the negative pressure peak increases exponentially, without bound. This means that in this high flow rate regime the bubble is pushed through more easily. Further tests on two tubes with different contraction diameters explain how the transition between the two regimes occurs. The first (positive) pressure peak is mostly due to the Laplace pressure, when the bubble is pushed through the contraction, as detailed in equation (1). As a first approximation, the Laplace pressure drop is

$$\Delta P_\sigma \approx \frac{4\sigma}{d}. \quad (4)$$

This is true for low flow rate situations, as seen, e.g., in figure 3, by the good agreement between measurements and simulation based on the quasi-stationary model. However, at higher flow rates the pressure drop  $\Delta P_{\text{fric}}$  due to friction can no longer be neglected. This contribution to the total pressure drop  $\Delta P_b$  is of magnitude

$$\Delta P_{\text{fric}} \approx \frac{128\mu\ell_{\text{con}}}{\pi d^4} Q. \quad (5)$$

The observed change in regime, where the positive pressure peak transient vanishes, therefore occurs when  $\Delta P_{\text{fric}} \approx \Delta P_\sigma$ . Using this together with the expressions for the flow rate,

$Q = \pi(d/2)^2 v$ , and the capillary number,  $Ca = \mu v/\sigma$ , the transition condition can be written as

$$Ca \approx \frac{d}{8\ell_{\text{con}}}. \quad (6)$$

Based on this equation, it is convenient now to define a rescaled capillary number  $Ca^*$  as

$$Ca^* \equiv \frac{8\ell_{\text{con}}}{d} Ca. \quad (7)$$

In terms of the rescaled capillary number, the transition happens at  $Ca^* \approx 1$ . Likewise, it is convenient to introduce the rescaled pressure drop amplitude of the pressure transient  $\Delta P^*$  as

$$\Delta P^* \equiv \frac{P(Q)}{P(0)}, \quad (8)$$

i.e., the ratio between the observed amplitude of the transient pressure drop at high flow rate  $Q$  and the amplitude of the positive pressure transient at negligible flow rate  $Q = 0$ .

In figure 8(b), the data of panel (a) are replotted using the rescaled variables  $\Delta P^*$  and  $Ca^*$ . The values of  $\ell_{\text{con}}$  can be determined by optical inspection of the contraction geometries, as a first estimate. In figure 8(b), we used values of  $\ell_{\text{con}}$  obtained by a linear regression between equation (5) and measurements of the viscous pressure drop. It is seen how the transition between the capillary pressure drop regime, with a large positive peak amplitude, and the viscous pressure drop regime, with a vanishing positive peak amplitude, occurs for  $Ca^* \approx 1$ . In other words, this criterion has practical implications: it discriminates between the case of bubbles clogging the flow through the contraction and the case of bubbles not clogging the flow.

## 5. Conclusion

An experimental study of a bubble passing through a microchannel contraction has been performed. Transient measurements have quantified the pressure and bubble shape during its motion through the contraction. The experiments were confronted with the simple theoretical model of quasi-static motion, and generally a good agreement was obtained. However, some deviations have been observed and discussed. The influence of the wetting angle has been studied. High-speed visualization reveals that some departures from the simulations are due to instabilities and breakup of the bubble. Experiments varying the flow rate show that two regimes govern the pressure transients when the bubble passes the contraction: a quasi-steady regime for low capillary number and a viscosity-influenced regime for non-negligible capillary numbers. A criterion based on a modified capillary number is proposed to discriminate between these two regimes, and it shows the existence of a critical flush velocity above which clogging by bubbles at contractions is avoided.

## Acknowledgments

This work was in part supported by the US National Science Foundation (CAREER award 35405). The glass tube contractions were manufactured by Rudy Schlott at Stony Brook: he passed away during our study. Despite the virulence of his illness, he mustered all his energies to continue working as a glassblower to virtually the bitter end.

**References**

- [1] Geschke O, Klank H and Telleman P (ed) 2004 *Microsystem Engineering of Lab-on-a-Chip Devices* (Weinheim: Wiley-VCH)
- [2] Tsai J and Lin L 2002 *Sensors Actuators A* **97–98** 665
- [3] Sammarco T S and Burns M A 1999 *AIChE J* **45** 350
- [4] Utada A S, Lorenceau E, Link D R, Kaplan P D, Stone H A and Weitz D A 2005 *Science* **308** 537
- [5] Anna S L, Bontoux N and Stone H A 2003 *Appl. Phys. Lett.* **82** 364
- [6] Garstecki P, Gitlin I, DiLuzio W, Kumacheva E, Stone H A and Whitesides G M 2004 *Appl. Phys. Lett.* **85** 2649
- [7] Gañán-Calvo A M and Gordillo J M 2001 *Phys. Rev. Lett.* **87** 274501
- [8] Gañán-Calvo A M 2004 *Phys. Rev. E* **69** 027301
- [9] Gravesen P, Branebjerg J and Søndergård Jensen O 1993 *J. Micromech. Microeng.* **3** 168
- [10] Elwenspoek M, Kannerubj T S, Miyake R and Fluitman J H J 1994 *J. Micromech. Microeng.* **4** 227
- [11] Jensen M J, Goranović G and Bruus H 2004 *J. Micromech. Microeng.* **14** 876
- [12] Batchelor G K 2000 *An Introduction to Fluid Dynamics (First Cambridge Math. Lib. Ed.)* (Cambridge: Cambridge University Press)
- [13] Mishra C and Peles Y 2005 *Phys. Fluids* **17** 013601
- [14] Bretherton F P 1961 *J. Fluid Mech.* **10** 97
- [15] Geng X, Yuan H, Oguz H N and Prosperetti A 2001 *J. Micromech. Microeng.* **11** 270
- [16] Redon C, Brochart-Wyart F and Rondelez F 1991 *Phys. Rev. Lett.* **66** 715
- [17] de Gennes P-G, Brochart-Wyart F and Quere D 2003 *Capillarity and Wetting Phenomena: Drops, Bubbles, Pearls, Waves* (New York: Springer)
- [18] Wang X S and Qiu H-H 2005 *Meas. Sci. Technol.* **16** 594
- [19] de Gennes P-G, Hua X and Levinson P 1989 *J. Fluid Mech.* **212** 55